

Predicting the synthesizability of inorganic crystals by bridging crystal graphs and phonon dynamics

Mei Ma(马梅), Wei Ma(马薇), Le Gao(高乐), Zong-Guo Wang(王宗国), and Hao Liu(刘昊)
Citation: Chin. Phys. B, 2026, 35 (**1**): 016101. DOI: 10.1088/1674-1056/ae0161
http://cpb.iphy.ac.cn; http://iopscience.iop.org/cpb

What follows is a list of articles you may be interested in

Atomic insights into topochemical fluorination and strong octahedral tilt in La_2CoO_4

Yuzhou He(何玉洲), Ting Lin(林挺), Shiyu Wang(王诗雨), Ang Gao(高昂), Ziang Meng(孟子昂), Tianping Ying(应天平), Zhiqi Liu(刘知琪), Lin Gu(谷林), Qinghua Zhang(张庆华), and Binghui Ge(葛炳辉)
Chin. Phys. B, 2025, 34 (**7**): 076102. DOI: 10.1088/1674-1056/adda0a

Exploring superconductivity in dynamically stable carbon-boron clathrates trapping molecular hydrogen

Akinwumi Akinpelu, Mangladeep Bhullar, Timothy A. Strobel, and Yansun Yao
Chin. Phys. B, 2025, 34 (**3**): 036103. DOI: 10.1088/1674-1056/ada757

Dendritic tip selection during solidification of alloys: Insights from phase-field simulations

Qingjie Zhang(张清杰), Hui Xing(邢辉), Lingjie Wang(王灵杰), and Wei Zhai(翟薇)
Chin. Phys. B, 2024, 33 (**9**): 096103. DOI: 10.1088/1674-1056/ad57ac

Strip method to construct a two-dimensional quasilattice with eight-fold symmetry

Weishen Huang(黄伟深) and Xiujun Fu(傅秀军)
Chin. Phys. B, 2024, 33 (**9**): 096102. DOI: 10.1088/1674-1056/ad51f2

Classification and structural characteristics of amorphous materials based on interpretable deep learning

Jiamei Cui(崔佳梅), Yunjie Li(李韵洁), Cai Zhao(赵偲), and Wen Zheng(郑文)
Chin. Phys. B, 2023, 32 (**9**): 096101. DOI: 10.1088/1674-1056/acd7d0

SPECIAL TOPIC — AI + Physical Science

Predicting the synthesizability of inorganic crystals by bridging crystal graphs and phonon dynamics

Mei Ma(马梅)[1], Wei Ma(马薇)[2], Le Gao(高乐)[3], Zong-Guo Wang(王宗国)[4], and Hao Liu(刘昊)[5,†]

[1] *School of Physics, Ningxia University, Yinchuan* 750021, *China*
[2] *School of Materials and New Energy, Ningxia University, Yinchuan* 750021, *China*
[3] *School of Information Engineering, Ningxia University, Yinchuan* 750021, *China*
[4] *Computer Network Information Center, Chinese Academy of Sciences, Beijing* 100083, *China*
[5] *School of Artificial Intelligence, Ningxia University, Yinchuan* 750021, *China*

(Received 17 June 2025; revised manuscript received 20 August 2025; accepted manuscript online 2 September 2025)

Accurately predicting the synthesizability of inorganic crystal materials serves as a pivotal tool for the efficient screening of viable candidates, substantially reducing the costs associated with extensive experimental trial-and-error processes. However, existing methods, limited by static structural descriptors such as chemical composition and lattice parameters, fail to account for atomic vibrations, which may introduce spurious correlations and undermine predictive reliability. Here, we propose a deep learning model termed integrating graph and dynamical stability (IGDS) for predicting the synthesizability of inorganic crystals. IGDS employs graph representation learning to construct crystal graphs that precisely capture the static structures of crystals and integrates phonon spectral features extracted from pre-trained machine learning interatomic potentials to represent their dynamic properties. Our model exhibits outstanding performance in predicting the synthesizability of low-energy unsynthesizable crystals across 41 material systems, achieving precision and recall values of 0.916/0.863 for ternary compounds. By capturing both static structural descriptors and dynamic features, IGDS provides a physics-informed method for predicting the synthesizability of inorganic crystals. This approach bridges the gap between theoretical design concepts and their practical implementation, thereby streamlining the development cycle of new materials and enhancing overall research efficiency.

Keywords: crystal synthesizability prediction, deep learning, graph learning, AI for science

PACS: 61.50.Ah, 63.20.D–, 81.05.Zx, 07.05.Mh

DOI: 10.1088/1674-1056/ae0161 **CSTR:** 32038.14.CPB.ae0161

1. Introduction

Designing novel inorganic functional materials that are readily synthesizable remains a central goal within the dynamic field of materials science. Recent advancements in high-performance computing, electronic structure calculations, and data-driven approaches have significantly accelerated the design of innovative inorganic functional materials, particularly in applications such as energy storage,[1,2] electrocatalysis[3] and photovoltaics.[4] These developments provide a solid theoretical foundation for discovering high-performance materials.

However, a significant challenge in the exploration of new crystalline materials lies in assessing their experimental synthesizability. Current predictions of synthesizability largely depend on empirical knowledge and heuristic judgments, leading to a notable deficiency in universal, efficient models for systematic assessment. This gap severely impedes the pace at which experimental material discovery and development can progress, making it essential to develop a model that can accurately and rapidly estimate crystal synthesizability.[5]

Despite recent advances, prevailing methodologies for predicting crystal synthesizability still face significant limitations. A prevalent approach relies on the minimum free energy principle, which indirectly addresses synthesizability by restricting the search to structures with total energy at the global minimum. However, such methods typically concentrate on ground-state structures.[6] In this context, Gibbs energy, a fundamental indicator of crystal stability, is extensively utilized.[7] Yet, obtaining Gibbs energy experimentally is challenging, as it requires thermodynamic measurements such as phase-transition temperatures and heat capacities, which limits the practical exploration of material stability and synthesizability.[8]

In the quest for new materials, the formation energy or the energy above the convex hull, derived from density functional theory (DFT) calculations performed at 0 K, is also employed as a preliminary estimate of synthesizability. However, studies involving high-throughput screening of numerous crystal structures using DFT have demonstrated that many theoretically low-energy geometries remain unsynthesized in experiments.[9] Consequently, relying solely on the energy

[†]Corresponding author. E-mail: liuhao@nxu.edu.cn

© 2026 Chinese Physical Society and IOP Publishing Ltd. All rights, including for text and data mining, AI training, and similar technologies, are reserved.

above the ground state cannot be deemed a reliable indicator of synthesizability.[6,9] As an alternative, the "amorphous limit" concept proposed by Aykol *et al.*[10] has attracted widespread attention because it provides a thermodynamic upper bound for the synthesizability of materials. Nonetheless, for each new composition, a new energy reference point must be established, making the method composition-dependent.

Although conventional methodologies have provided valuable insights into materials synthesis, the correlations between candidate materials and the physical processes influencing their synthesizability have yet to be adequately elucidated. This unresolved complexity has driven the development of machine learning-based predictive frameworks that identify latent patterns within expansive datasets. For instance, SynthNN[11] employed deep networks to learn the relationship between elemental composition and synthesizability, enabling rapid chemical space exploration but failing to distinguish polymorphs. Moving beyond composition-based approaches, Davariashtiyani *et al.*[12] encoded crystal structures as voxel images and employed a convolutional neural network to extract spatial features for synthesizability prediction, although this voxelization process may sacrifice certain precise structural details. Zhu *et al.*[13] combined real-space and reciprocal-space descriptors through discrete Fourier transforms to incorporate periodicity. Meanwhile, graph neural networks (GNNs) have emerged as a powerful approach for structure-aware synthesizability predictions. By pioneering the use of graph representations in materials informatics, the crystal graph convolutional neural network (CGCNN)[14] laid the foundation for subsequent models such as crystal-likeness scores (CLscore).[15] Notably, these approaches predominantly rely on mapping static structural descriptors of crystals to synthesizability while neglecting the intrinsic dynamical properties associated with atomic vibrations. This incomplete feature representation introduces systematic uncertainties that may lead to spurious or inaccurate correlations, ultimately compromising both the reliability and predictive accuracy of the models.

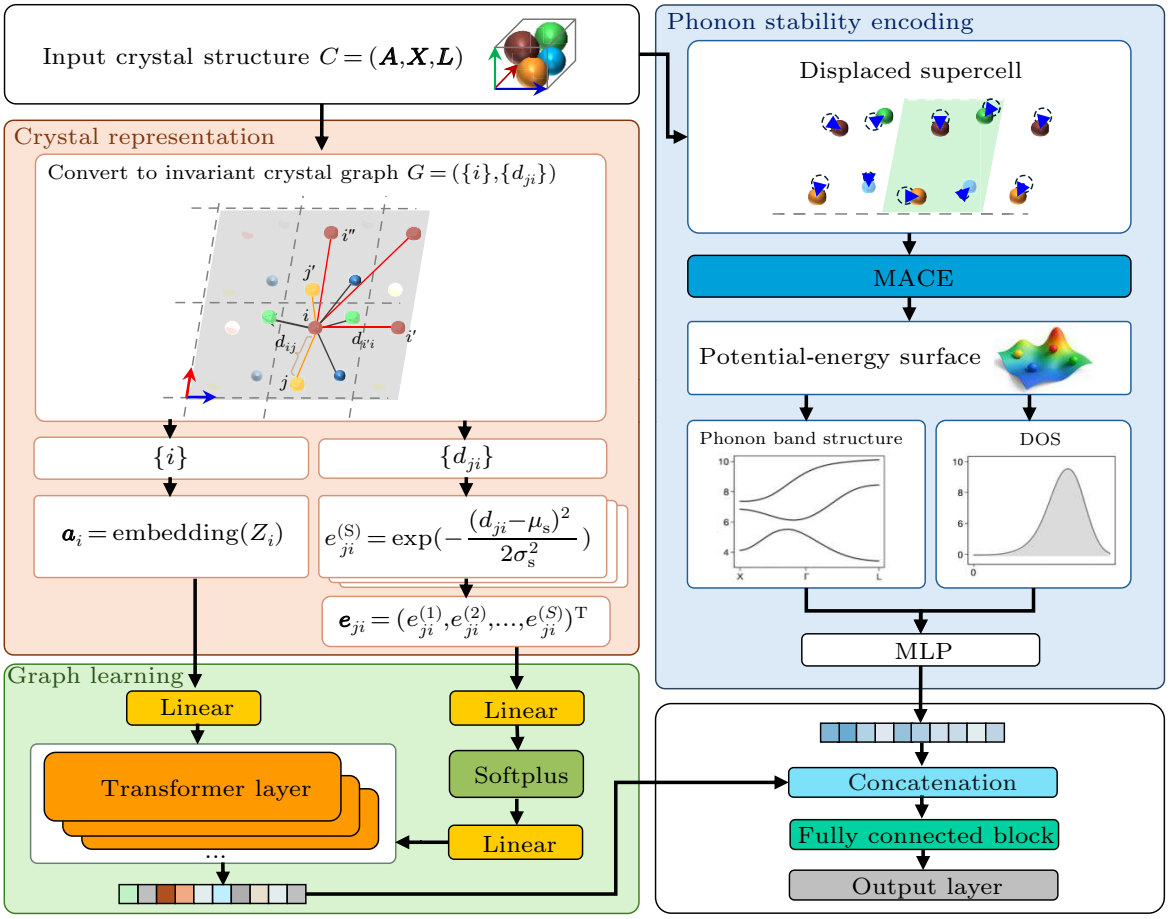


Fig. 1. Overview of the IGDS framework. The crystal structure with N atoms per unit cell is converted into an invariant crystal graph via the crystal representation module. Based on this representation, the graph learning module utilizes t transformer layers with H attention heads to perform message passing. Concurrently, the phonon stability encoding module employs the MACE model to compute atomic-level energy contributions and predict forces. Supercell atomic displacements are combined with forces predicted by the machine-learning model to derive force constants, which are then diagonalized in the dynamical matrix to obtain phonon spectra. By integrating these dynamic features with crystal graph representations, the model effectively captures the interplay between structural and dynamic properties, enhancing its ability to predict synthesizability and identify experimentally realizable materials.

Here, we introduce an innovative integrated graph and dynamical stability (IGDS) approach, a deep learning model designed to precisely predict the synthesizability of crystalline materials (Fig. 1). To inherit constraints of the underlying physics,[16] IGDS leverages graph representation learning to construct an E(3)-invariant crystal graph that explicitly encodes the unique periodicity of the crystal, ensuring that its feature representation remains invariant under translation, rotation, and reflection. IGDS ensures periodic invariance by incorporating atoms in adjacent unit cells into the crystal graph to explicitly encode the lattice periodicity. Given that metastable materials, although thermodynamically unstable, can nonetheless be synthesized under certain conditions and remain dynamically stable,[17] a comprehensive predictive model for crystal synthesizability should also incorporate atomic vibrational dynamics. These dynamical stability features are critical for capturing the nuanced interplay between thermodynamic and kinetic factors that govern their formation. Specifically, we extracted phonon spectral features by computing the force constant matrix from small atomic displacements using a pre-trained interatomic potential and diagonalizing the dynamical matrix. Subsequently, the crystal graph features and dynamical stability features were integrated to effectively capture the complex interactions between static structures and dynamical properties, enhancing the efficiency of feature learning. Evaluation results on the materials project (MP)[18] dataset demonstrate the effectiveness of our IGDS model in precisely predicting crystal synthesizability. Furthermore, the quantitative visualization highlights the model's exceptional performance, particularly in identifying low-energy unsynthesizable crystals, underscoring its robustness and precision.

2. Methodology

Predicting inorganic crystal synthesizability requires atomic-scale modeling and adherence to crystallographic symmetry constraints in deep learning frameworks. IGDS inherits the fundamental physical constraints of crystals by constructing invariant features through the crystal graph. This representation enables a more comprehensive and accurate understanding of the geometrical properties of crystals, allowing the model to capture essential characteristics crucial for downstream prediction. Furthermore, IGDS incorporates both static structural features and phonon features reflecting the dynamic behavior of crystals at 0 K. The structural features are augmented with dynamic stability features to better identify potentially synthesizable crystals. In this section, we first provide a detailed introduction to crystal representation in Subsection 2.1. Then, in Subsection 2.2, we present the graph learning module for capturing the static structural features of crystals. Finally, Subsections 2.3 and 2.4 present the phonon stability encoding module and the training details, respectively.

2.1. Crystal representation

Unlike molecules, crystal structures exhibit periodic arrangements in three-dimensional space. They consist of a unit cell along with an atomic basis, which is the set of atoms associated with that unit cell.

A unit cell containing N atoms is defined as the triplet $C = (\boldsymbol{A}, \boldsymbol{X}, \boldsymbol{L})$, where $\boldsymbol{A} = [\boldsymbol{a}_1, \boldsymbol{a}_2, \ldots, \boldsymbol{a}_N]$ is the feature matrix whose columns $\boldsymbol{a}_i \in \mathbb{R}^{d_a}$ (for $i = 1, 2, \ldots, N$) are d_a-dimensional atomic feature vectors and $\boldsymbol{X} = [\boldsymbol{x}_1, \boldsymbol{x}_2 \ldots, \boldsymbol{x}_N]$ is the position matrix whose columns $\boldsymbol{x}_i \in \mathbb{R}^3$ represent the atomic positions in three-dimensional Cartesian space. The periodicity of the crystal is described by the lattice matrix $\boldsymbol{L} = [\boldsymbol{l}_1, \boldsymbol{l}_2, \boldsymbol{l}_3] \in \mathbb{R}^{3\times3}$. The infinite crystal is formed by translating the unit cell along its lattice vectors. For each translation vector $\boldsymbol{b} \in \mathbb{Z}^3$, the atomic positions become $\boldsymbol{x}'_i = \boldsymbol{x}_i + \boldsymbol{L}\boldsymbol{b}$. Thus, the entire periodic crystal structure can be represented as $\left\{ (\boldsymbol{a}_i, \boldsymbol{x}'_i) \,\middle|\, i = 1, 2, \ldots, N,\ \boldsymbol{b} \in \mathbb{Z}^3 \right\}$.

For a given crystal, we represent the atom i in the unit cell as a node i and extend this representation to include all its periodic images in the infinite three-dimensional space. Edges are defined based on the geometric distances between nodes, as distance reflects the intensity of physical interactions and the spatial relationships between atoms — factors that are crucial for capturing the local interactions in crystal structures.[19,20] To ensure the translational invariance of the crystal graph, it is necessary to consider multiple adjacencies resulting from the translation of atoms across different lattice periods when constructing edges between nodes. Therefore, for the central node i, we use the set $\boldsymbol{D}^o_{ji}$ to determine the edges connecting node j to it. The formula is as follows:

$$\boldsymbol{D}_{ji} = \left\{ d_{ji} \,\middle|\, d_{ji} = \left\| \boldsymbol{x}'_j - \boldsymbol{x}_i \right\|_2,\ \boldsymbol{x}'_j = \boldsymbol{x}_j + \boldsymbol{L}\boldsymbol{b}, \boldsymbol{b} \in \mathbb{Z}^3 \right\}, \quad (1)$$

$$\boldsymbol{D}^o_{ji} = \left\{ d_{ji} \,\middle|\, d_{ji} \in \mathrm{Sort}\left(\boldsymbol{D}_{ji}\right)[:o] \right\}, \quad (2)$$

$$\varepsilon_{ji} = \left\{ \{j, i\} \,\middle|\, d_{ji} \in \boldsymbol{D}^r_{ji} \right\}, \quad (3)$$

where $\mathrm{Sort}\left(\boldsymbol{D}_{ji}\right)[:o]$ denotes the operation of selecting the o nearest elements based on the k-nearest neighbor distance metric, ε_{ji} represents the set of edges from atom i to atom j and its duplicates j'.

Furthermore, lattice vectors $\boldsymbol{l}_i \in \boldsymbol{L}$ are key factors describing the periodic pattern of crystals, determining many physical properties of the crystal. To accurately distinguish the symmetric geometric features of different crystalline materials, it is crucial to explicitly embed these periodic patterns into the crystal graph. However, most existing graph neural network approaches for crystals, including CGCNN,[14] have not explicitly considered this periodic pattern embedding. To address this limitation, a straightforward approach

is to use the lattice vectors derived from the input lattice matrix to define additional edges for the crystal graph. Nevertheless, this approach depends on the chosen lattice basis. Different lattice bases — e.g., $(\boldsymbol{l}_1,\boldsymbol{l}_2,\boldsymbol{l}_3)$ versus $(\boldsymbol{l}_1+\boldsymbol{l}_2,\boldsymbol{l}_2,\boldsymbol{l}_3)$ — can describe the same lattice yet yield different graph representations, as they are related by a unimodular transformation with $\det(T)=1$.[21] To ensure periodic invariance, we connect each atom to its corresponding periodic duplicate in adjacent unit cells, thereby explicitly encoding the lattice's repeating spacings via the geometric distances between these inter-cell atomic pairs. Specifically, for each atom i and its set P of periodic images (including duplicates), we select three edge vectors as follows. First, we identify the closest periodic duplicate

$$i' = \text{argmin}_{j\in P\setminus\{i\}} \|\boldsymbol{x}_{i'} - \boldsymbol{x}_i\|_2, \tag{4}$$

the corresponding edge vector is defined as $\boldsymbol{r}_{i'i} = \boldsymbol{x}_{i'} - \boldsymbol{x}_i$. Since i' is a periodic duplicate of i, this vector corresponds to a self-loop edge at node $\boldsymbol{i}$, which is $d_{i'i} = \|\boldsymbol{r}_{i'i}\|_2$.

Next, we choose the second duplicate by selecting the closest candidate distinct from i and i', ensuring its edge vector is not collinear with $\boldsymbol{r}_{i'i}$. The specific expression is

$$i'' = \text{argmin}_{j\in P\setminus\{i,i'\}} \|\boldsymbol{x}_{i''} - \boldsymbol{x}_i\|_2 \text{ subject to } \boldsymbol{r}_{i''i} \notin \text{span}\{\boldsymbol{r}_{i'i}\}. \tag{5}$$

Finally, we select a third duplicate from $P\setminus\{i,i',i''\}$ such that its edge vector is linearly independent of both $\boldsymbol{r}_{i'i}$ and $\boldsymbol{r}_{i''i}$

$$i''' = \text{argmin}_{j\in P\setminus\{i,i',i''\}} \|\boldsymbol{x}_{i'''} - \boldsymbol{x}_i\|_2 \text{ with } \boldsymbol{r}_{i'''i} \notin \text{span}\{\boldsymbol{r}_{i'i}, \boldsymbol{r}_{i''i}\}, \tag{6}$$

where $\text{span}\{\boldsymbol{r}_{i'i}, \boldsymbol{r}_{i''i}\} = \{\alpha\boldsymbol{r}_{i'i} + \beta\boldsymbol{r}_{i''i} | \alpha,\beta \in \mathbb{R}\}$.

Based on the magnitudes of vectors $\boldsymbol{r}_{i'i}$, $\boldsymbol{r}_{i''i}$, $\boldsymbol{r}_{i'''i}$, $\boldsymbol{r}_{i'i}+\boldsymbol{r}_{i''i}$, $\boldsymbol{r}_{i''i}+\boldsymbol{r}_{i'''i}$, and $\boldsymbol{r}_{i'''i}+\boldsymbol{r}_{i'i}$, we effectively embed the lattice's periodic and directional information into the crystal graph via self-loops, as shown in Fig. 2.

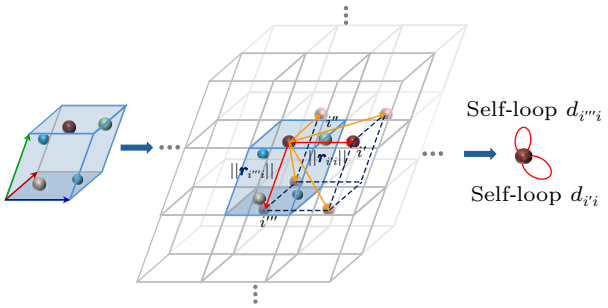


Fig. 2. Graph representation of the crystal structure. The edge vectors connecting atom i to its periodic duplicates, along with the pairwise sums of these vectors, are used to form self-loops that explicitly encode the lattice's repeating pattern and directional information.

Based on our method for constructing the crystal graph, the node and edge features are specified as follows:

Node embeddings Each node i is represented by its atomic number Z_i, which is transformed into a continuous vector $\boldsymbol{a}_i$ using the embedding function derived from CGCNN.[14] Formally, this is expressed as

$$\boldsymbol{a}_i = \text{embedding}(Z_i). \tag{7}$$

Edge embeddings The Euclidean distance d_{ji} between nodes i and j of the crystal graph is mapped to a continuous vector using a set of S Gaussian radial basis functions (RBFs).[22] Each component $e_{ji}^{(s)}$ of this vector is computed as

$$e_{ji}^{(s)} = \exp\left(-\frac{(d_{ji}-\mu_s)^2}{2\sigma_s^2}\right), \tag{8}$$

where $s = 1,2,\ldots,S$. The centers $\{\mu_s\}_{s=1}^{S}$ are uniformly spaced between 0 and a cutoff distance $d_{\max}$, and the width σ_s is fixed as $\sigma_s = \frac{d_{\max}}{S}$. The full embedding vector is $\boldsymbol{e}_{ji} = \left(e_{ji}^{(1)}, e_{ji}^{(2)}, \ldots, e_{ji}^{(S)}\right)^{\mathrm{T}}$.

Leveraging the previously defined node and edge features, the proposed crystal graph construction method ensures $E(3)$ invariance and periodic invariance. Specifically, edge features are derived solely from the Euclidean distance between atomic pairs, which is invariant under $E(3)$ transformations such as translation, rotation, and reflection in three-dimensional space. Node features, defined by atomic types, are independent of positional or orientational information, further reinforcing invariance to geometric transformations. Furthermore, edge embeddings encode lattices of different sizes and orientations through a novel neighbor selection strategy and effective utilization of geometric distances across periodic boundaries. This approach explicitly captures the periodic patterns inherent in crystal structures, enabling an accurate representation of the infinite periodicity of crystals. Moreover, periodic boundary conditions are explicitly incorporated during graph construction, ensuring that both edge connectivity and distance computations are consistent under periodic tiling of the unit cell. As a result, the graph structure and its features are invariant under periodic extensions, thereby guaranteeing periodic invariance.

2.2. Graph learning

We denote the invariant crystal graph constructed based on Subsection 2.1 as $G = (\{i\},\{d_{ji}\})$. In the transformer layer, we leverage the node features $\boldsymbol{a}_i$ and $\boldsymbol{a}_j$ together with edge features $\boldsymbol{e}_{ji}$ to transmit information from a neighboring node j to the central node i. The messages from all neighboring nodes are then aggregated to update the node feature $\boldsymbol{a}_i$ at the t-th layer.

The message from node j to node i is composed of the corresponding query $\boldsymbol{q}_{ji}$, key $\boldsymbol{k}_{ji}$, and value features $\boldsymbol{v}_{ji}$, which are defined as follows:

$$\boldsymbol{q}_{ji}^{h} = \left(\text{Linear}_{\text{Q}}\left(\boldsymbol{a}_i^t\right)\right) \left|\left(\text{Linear}_{\text{Q}}\left(\boldsymbol{a}_i^t\right)\right)\right| \left(\text{Linear}_{\text{Q}}\left(\boldsymbol{a}_i^t\right)\right), \tag{9}$$

$$\boldsymbol{k}_{ji}^{h} = \left(\text{Linear}_{\text{K}}\left(\boldsymbol{a}_{i}^{t}\right)\right) \mid \left(\text{Linear}_{\text{K}}\left(\boldsymbol{a}_{j}^{t}\right)\right) \mid \left(\text{Linear}_{\text{E}}\left(\boldsymbol{e}_{ji}^{h}\right)\right), \quad (10)$$

$$\boldsymbol{v}_{ji}^{h} = \left(\text{Linear}_{\text{V}}\left(\boldsymbol{a}_{i}^{t}\right)\right) \mid \left(\text{Linear}_{\text{V}}\left(\boldsymbol{a}_{j}^{t}\right)\right) \mid \left(\text{Linear}_{\text{E}}\left(\boldsymbol{e}_{ji}^{h}\right)\right), \quad (11)$$

$$\boldsymbol{\alpha}_{ji}^{h} = \frac{\boldsymbol{q}_{ji}^{h} \circ \boldsymbol{k}_{ji}^{h}}{\sqrt{d_{\boldsymbol{k}_{ji}^{h}}}}, \quad (12)$$

$$\boldsymbol{m}_{ji}^{h} = \text{sigmoid}\left(\text{LNorm}\left(\boldsymbol{\alpha}_{ji}^{h}\right)\right) \circ \text{Linear}_{\text{update}}\left(\boldsymbol{v}_{ji}^{h}\right), \quad (13)$$

where $\text{Linear}_{\text{Q}}(\cdot)$, $\text{Linear}_{\text{K}}(\cdot)$, $\text{Linear}_{\text{V}}(\cdot)$, and $\text{Linear}_{\text{E}}(\cdot)$ denote the linear transformations for query, key, value, and edge features, respectively. The symbol "|" indicates concatenation, while "$\circ$" represents the Hadamard product. Here, $d_{\boldsymbol{k}_{ji}^{h}}$ is the dimensionality of $\boldsymbol{k}_{ji}^{h}$, $\text{LNorm}(\cdot)$ stands for the layer normalization operation, and $\text{Linear}_{\text{update}}(\cdot)$ is the linear transformation used to compute the updated message.

After obtaining coefficients $\boldsymbol{\alpha}_{ji}^{h}$ and the message $\boldsymbol{m}_{ji}^{h}$ for the h-th edge between j and i, we aggregate information from node i's neighborhood over multiple edges to compute the aggregated message $\boldsymbol{m}_{i}$. This message is then used to update the node feature $\boldsymbol{a}_{i}^{t}$ at the next layer

$$\begin{aligned} \boldsymbol{m}_{i} &= \sum_{j \in N_i} \sum_{h} \text{LNorm}\left(\text{LNmsg}\left(\boldsymbol{m}_{ji}^{h}\right)\right), \\ \boldsymbol{a}_{i}^{t+1} &= \text{LN}_{\text{f}}\left(\boldsymbol{a}_{i}^{t}\right) + \sigma\left(\text{BN}\left(\boldsymbol{m}_{i}\right)\right), \end{aligned} \quad (14)$$

where $\text{LNmsg}(\cdot)$ and $\text{LN}_{\text{f}}(\cdot)$ are the linear transformations to update the messages on edges and the old atom features, respectively. $\text{BN}(\cdot)$ indicates batch normalization, and $\sigma(\cdot)$ is the softplus activation function.

2.3. Phonon stability encoding

Inspired by metastable materials that are not thermodynamically stable but may still form under certain synthesis conditions and remain dynamically stable,[17] we incorporate the dynamic stability features of crystals into the model. Dynamic stability reflects the behavior of crystals during the synthesis process, enabling the model to assess crystal stability from multiple perspectives. To accurately capture the dynamic stability of crystals, it is essential to consider phonons, as they play a critical role in determining dynamic stability.[23] In the harmonic approximation, a crystal is dynamically stable if all phonons have real and positive frequencies, which are determined based on the restoring forces acting on atomic displacements.[24] However, DFT-based phonon calculations are computationally expensive, particularly for large or complex structures, as they require numerous force evaluations across multiple displaced configurations.[25] To overcome this limitation, we employ a pre-trained machine learning potential model (MACE-MP-0,[26] which predicts restoring forces using the MACE framework[27] and is trained on the MPtrj[28] dataset) to efficiently predict restoring forces, enabling high-throughput phonon computations.

Specifically, phonon spectral features are computed by combining the finite displacement method with MACE-MP-0[26] and PHONOPY.[29,30] A supercell is constructed to capture interatomic interactions beyond the base unit cell. Within this framework, small atomic displacements (0.01 Å) are applied to each symmetry-inequivalent atom to enable MACE-MP-0 to predict the restoring forces acting on all atoms for each displaced configuration. These forces in response to the known displacements provide the information needed to compute the force constants, which are essentially the second derivatives of the potential energy. Based on these results, the force constants are used to construct and diagonalize the dynamical matrix with PHONOPY,[29,30] thereby yielding the phonon frequencies and vibrational modes.

From the computed phonon spectra, we extract features indicative of dynamical stability from both the phonon band structure and the density of states (DOS). In the phonon band structure, the presence and magnitude of negative frequencies serve as primary indicators of potential dynamical instability. To ensure consistent feature dimensions across different crystal structures, we uniformly sample phonon frequencies along high-symmetry paths and concatenate them into a fixed-length vector. For the phonon DOS, the positive-frequency range is divided into equal intervals, and the integrated density within each interval is calculated to reflect the distribution of vibrational modes. Finally, the phonon dynamic features are obtained by concatenating the extracted band structure and DOS features.

2.4. Model implementation and training

The IGDS model architecture employs 128-dimensional node embeddings derived from CGCNN atomic embeddings. Edge embeddings are constructed by mapping the Euclidean distances between nodes into 128-dimensional vectors using 128 Gaussian radial basis functions (RBFs) with centers uniformly distributed over the range 0 Å to 8.0 Å. The graph learning module comprises five transformer layers, each with four attention heads, where the $\boldsymbol{q}_{ji}$, $\boldsymbol{k}_{ji}$, and $\boldsymbol{v}_{ji}$ vectors in each head have an embedding dimension of 128. For the pretrained model MACE-MP-0, all key parameters are kept at their default MACE settings. Among the three MACE-MP-0 variants ($L = 0, 1, 2$ for small, medium, and large models, respectively), we use the medium variant.

For training, the IGDS model is implemented in PyTorch and trained on the Materials Project dataset using an 80:10:10 split for training, validation, and testing, respectively. Optimization is performed with the Adam optimizer[31] incorporating a weight decay[32] of 1×10^{-5}, together with a one-cycle learning rate scheduler.[33] The cross-entropy loss is adopted as the objective function.

3. Results

In this section, we conduct a comprehensive evaluation of the IGDS model from multiple perspectives. Specifically, Subsection 3.2 compares the performance of our model on different datasets and contrasts it with other methods, Subsection 3.3 presents a case study demonstrating the application of IGDS in predicting specific materials, Subsection 3.4 explores the comparison between IGDS and energy-based metrics, and Subsection 3.5 evaluates the effectiveness of the model in identifying dynamic stability features.

3.1. Dataset description

The synthesizability of materials is often influenced by experimental conditions. However, most existing databases lack detailed information on these factors. In this work, we utilize the MP dataset (v2018.06.01),[34] which comprises 69239 crystals obtained from the MP.[18] Entries in the inorganic crystal structure database (ICSD)[35] are assigned unique identifiers called ICSD IDs and serve as evidence of experimental validation; that is, a crystal with one or more ICSD IDs has been successfully synthesized. Consequently, we treat synthesizability prediction as a special case of open set recognition (OSR),[36] regarding the materials with ICSD IDs as known and materials without ICSD IDs as unseen samples. By linking the ICSD IDs within the MP database, we adopt the approach presented by Yan *et al.*[37] as the baseline for developing our crystal synthesizability prediction model, IGDS. By employing the graph neural network to extract crystal structural information and integrating it with dynamical stability features computed by a pre-trained machine learning interatomic potential, IGDS enhances inter-class variance and enables implicit discrimination of unseen, unsynthesizable materials.

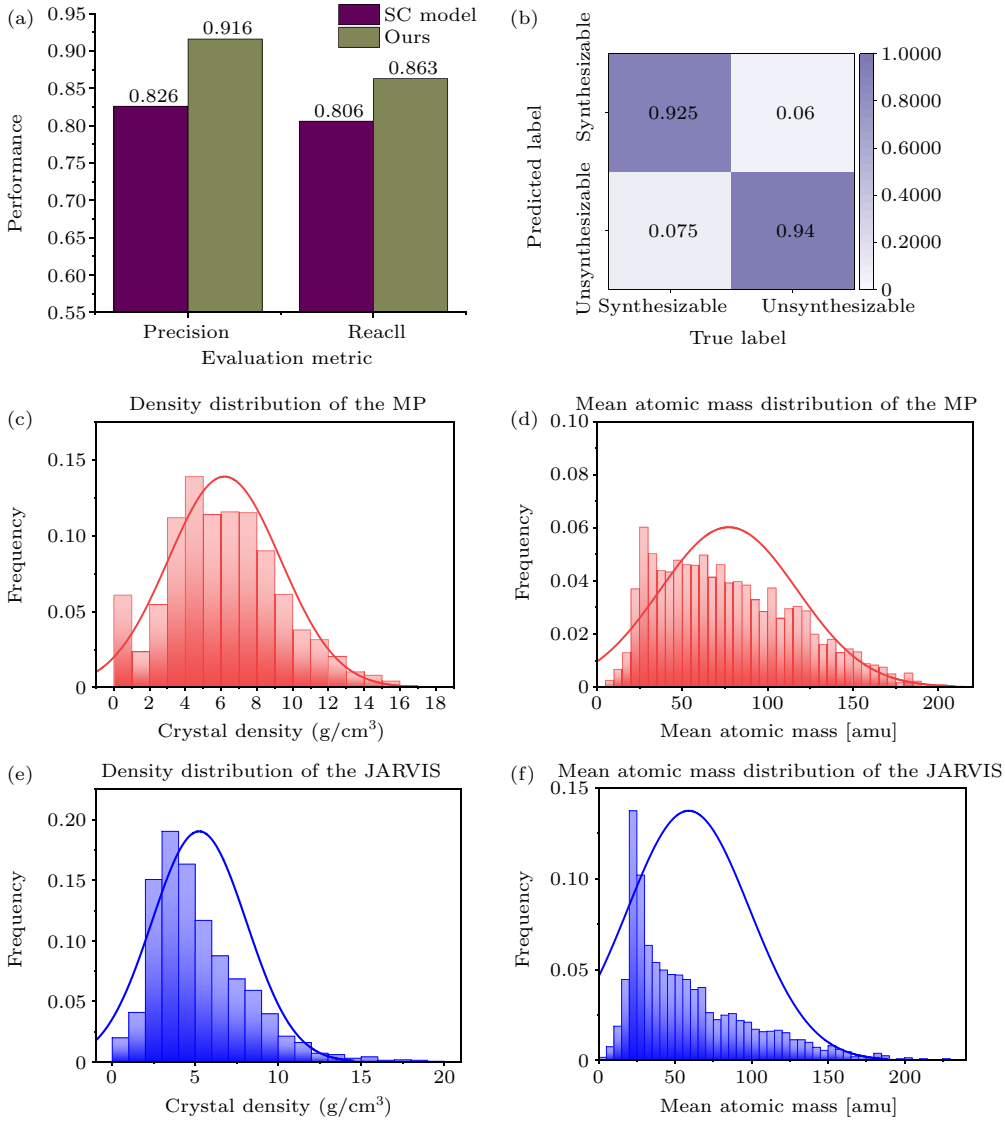


Fig. 3. Performance evaluation of the IGDS model. (a) Comparison of prediction accuracy between IGDS and the SC model[13] for ternary compounds. (b) Confusion matrix illustrating the performance of the IGDS classification model; entries along the main diagonal represent correct predictions, while off-diagonal entries indicate misclassifications. (c) and (d) Distributions of density and mean atomic mass for the MP dataset. (e) and (f) Corresponding distributions for the JARVIS dataset.

3.2. Model performance evaluation

In Fig. 3(a), the performance of our IGDS model on ternary compounds is summarized based on precision and recall. The results indicate that, when evaluated on the same dataset (MP v2021.03.22),[13] our model achieves a 9% increase in precision and a 5.7% improvement in recall on the ternary dataset, outperforming the method proposed by Zhu *et al.*[13] These remarkable improvements highlight the superiority of our model in identifying and predicting synthesizable compounds. The increase in precision indicates that a higher percentage of the compounds predicted as synthesizable by our model are experimentally verified, while the improvement in recall reflects the model's enhanced ability to correctly identify a greater proportion of truly synthesizable compounds. These results strongly emphasize the effectiveness of our IGDS model in capturing the intricate relationships between crystals and their synthesizability. This not only validates the advanced nature of our model, but also offers great potential for its application in practical materials synthesis research and development.

To demonstrate the robustness of our IGDS model, we conduct a detailed comparison of the physical property distributions for the MP[18] and JARVIS[38] datasets, using 3000 randomly sampled entries from each dataset to ensure statistical representativeness. Figures 3(c)–3(f) illustrate the distribution of the two datasets in terms of crystal density and mean atomic mass. Specifically, the sample density of the JARVIS dataset is primarily concentrated at 2–10 g/cm^3, indicating a more homogeneous crystal structure, whereas the MP dataset shows a wider density distribution (about 2.5–100 g/cm^3) and a more dispersed mean atomic mass distribution, reflecting its chemical compositional diversity. It is noteworthy that, despite the higher complexity and wider range of physical properties of the MP dataset, the accuracy of our IGDS model trained on the MP dataset (0.932) is comparable to its performance on the JARVIS dataset (0.929). By comparing the distributional properties of different datasets, we verify that the model maintains high performance in the face of varying physical and chemical properties, thus indicating good generalization ability. This is further demonstrated in Fig. 3(b), which presents the model's prediction results in the form of a confusion matrix.

3.3. Case study: crystal synthesizability prediction

This section aims to validate the performance of our crystal synthesizability prediction model on different categories of crystal materials.

Figure 4 presents the synthesizability predictions for a specific subset of samples sourced from prior work.[39] The selected samples, which cover various thermoelectric and electronic materials such as Cu_2Se_2Tl, P_2SnZ, CdP_2Sn, and $Li_7La_3(SnO_6)_2$, are visualized using t-SNE dimensionality reduction, with each sample annotated by its predicted probability of being synthesizable. Furthermore, to verify the reliability of our model, we also perform predictions on the synthesizability of crystals that have been experimentally confirmed to be synthesizable.

Figure 4 also displays the prediction results for these samples, which include some crystals reported in experiments but lacking ICSD IDs in the MP database (e.g., $Cs_2AgSbBr_6$,[40] $Cs_2InAgCl_6$,[41] and $BaHfO_3$[42]).

Overall, IGDS not only effectively predicts the synthesizability of different categories of crystals, but its prediction results are also highly consistent with existing experimental findings. This demonstrates the significant potential of our model for practical applications.

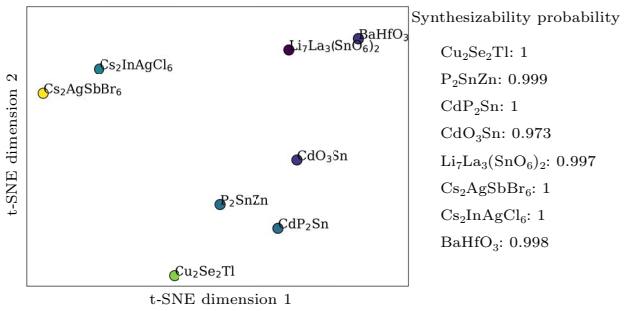


Fig. 4. The t-SNE visualization of structural features extracted using the proposed IGDS model. (Left) The 2D embeddings are colored according to the standardized mean atomic number of each material. (Right) Predicted synthesizability probabilities for the selected materials.

3.4. Comparison with energy-based synthesizability metrics

The stability skyline model[10] proposes a simple energy-based metric to assess the synthesizability of crystals. It adopts the DFT energy of the amorphous solid phase as the thermodynamic upper limit for crystalline materials considered synthesizable. Nevertheless, as shown in Fig. 5(a), this model demonstrates lower accuracy in predicting low-energy, unsynthesized crystals. To rigorously evaluate the accuracy of our model in this challenging scenario, we adopt the same 41 material systems used in the stability skyline model.[10] We then visualize the prediction performance of our model, with energy represented on the x-axis (see Fig. 5(b)). The results show that, in the low-energy region, our model achieves a substantial improvement in predicting unsynthesized crystals. In contrast, for high-energy synthesized crystals, both models perform similarly, with no significant difference. Upon analyzing the data for high-energy crystals within the 41 material systems, we observe that 30 crystals fall within the energy range of 0.6 eV/atom to 0.7 eV/atom, whereas only 8 crystals are found in the range of 0.8 eV/atom to 1.0 eV/atom, as shown in Fig. 5(d). This imbalance in the high-energy region likely contributes to the reduced prediction accuracy of our model in that domain and represents a key focus for future investigation.

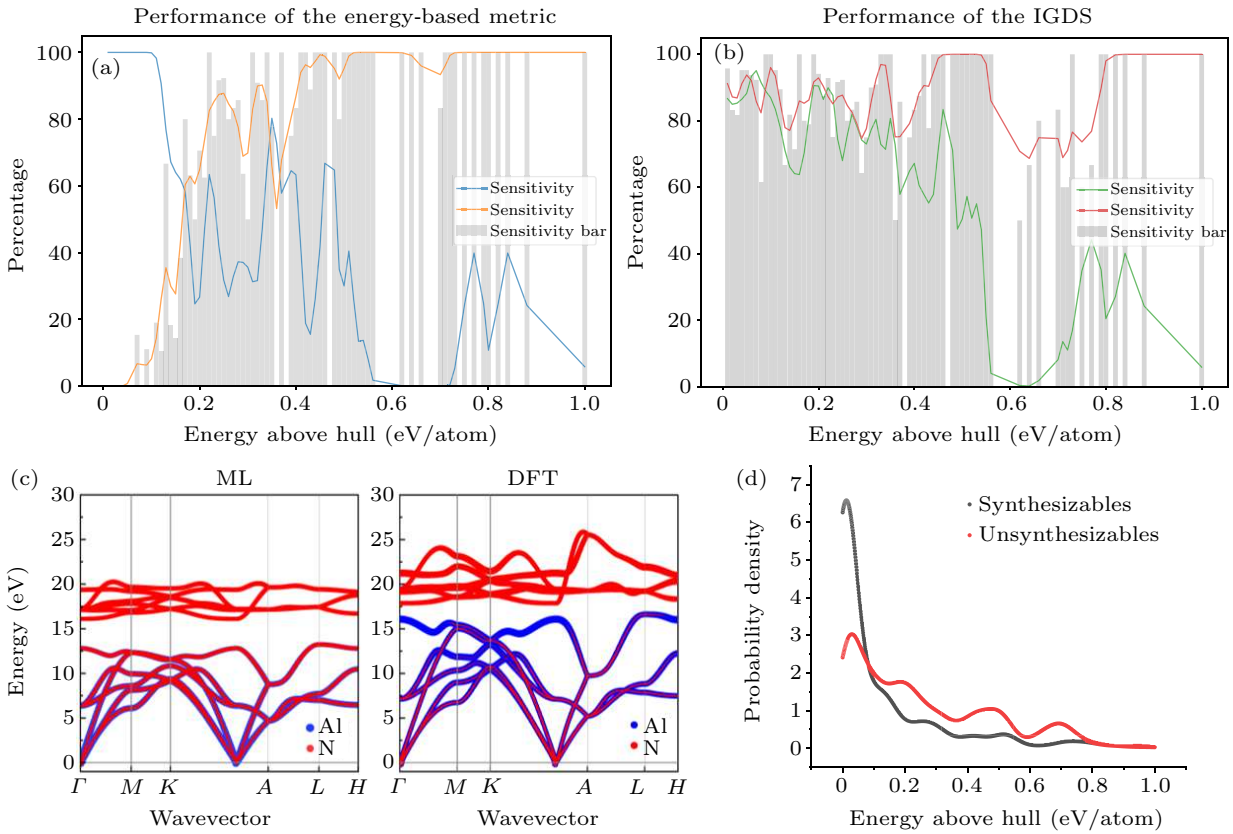


Fig. 5. Assessment of crystal energy-based synthesizability metrics. (a) and (b) Comparison of synthesizability prediction performance between the stability skyline model and our proposed IGDS model across 41 material systems, using energy values from the MP[18] as the *x*-axis. (a) The stability skyline model defines synthesizability based on the amorphous energy limit,[22] classifying all crystals with lower energy as synthesizable. This approach leads to high false positive rates for low-energy, unsynthesizable crystals and reduced accuracy for high-energy cases. (b) In contrast, our model demonstrates improved sensitivity (accurate identification of synthesizable crystals) and specificity (accurate identification of unsynthesizable crystals), providing more reliable predictions across the entire energy spectrum. (c) Evaluation of the dynamical features predicted by our model. (d) Probability distribution of the energy for the crystals predicted as synthesizable by our model.

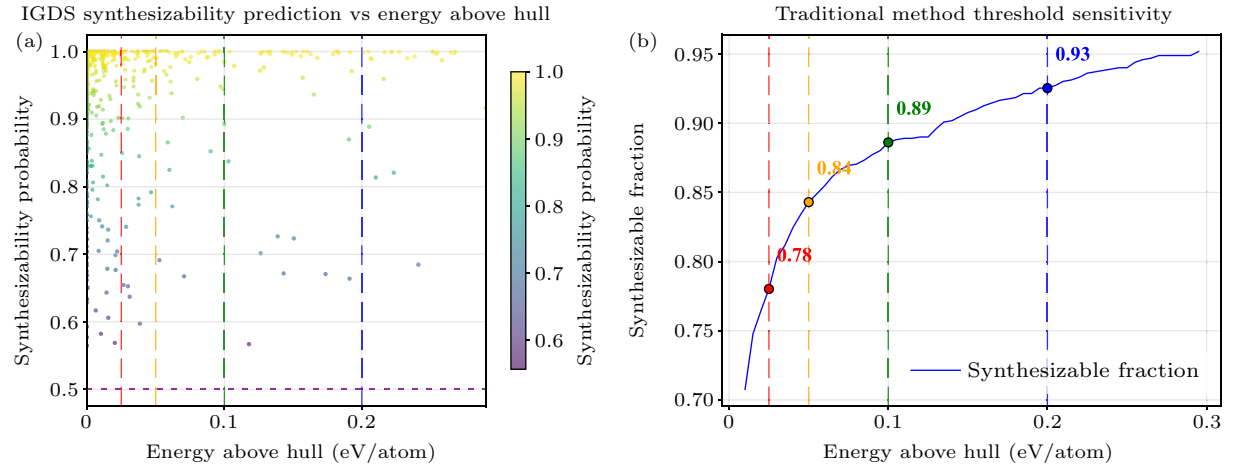


Fig. 6. Comparison of IGDS-predicted synthesizability and E_{hull} values for MP materials. (a) Correlation between IGDS probabilities and E_{hull} values. (b) Sensitivity of conventional E_{hull} thresholds and agreement with IGDS predictions.

To further demonstrate the performance of our method, we analyze 1019 materials from the MP dataset (v2021.03.22) that are predicted by IGDS to be synthesizable and compare their predictions with the corresponding E_{hull} values from the traditional approach. As shown in Fig. 6(a), IGDS provides continuous probabilistic predictions, whereas the traditional method relies on arbitrary binary thresholds (e.g., 0.025–0.2 eV/atom). Such continuous outputs enable the detection of subtle differences in synthesizability and offer quantitative guidance for experimental prioritization. Figure 6(b) presents the classification sensitivity of the conventional E_{hull} method at four cutoffs (0.025 eV/atom, 0.05 eV/atom, 0.1 eV/atom, 0.2 eV/atom). A small change in the threshold from 0.025 eV/atom to 0.05 eV/atom results in a 6% change

in classification outcomes. Importantly, even under the most stringent conventional threshold ($E_{\text{hull}} \leq 0.026$ eV/atom), our method maintains a 78% agreement while also identifying potential synthesizable candidates that might be missed by the conventional approach. These results confirm that IGDS provides a more accurate and reliable assessment of synthesizability than relying solely on E_{hull} thresholds.

3.5. Evaluation of dynamic stability feature accuracy

In this section, we conduct a comprehensive evaluation of the dynamical features predicted by our model, focusing particularly on the comparison of phonon properties against ab initio data. Utilizing the experimental setup outlined in MACE-MP-0,[26] we assess the reliability of the phonon features predicted by MACE-MP-0 (hereafter referred to as MACE). As shown in Fig. 7, we compare MACE with two other machine-learning interatomic potentials. Figure 7(a) demonstrates that MACE produces minimal phonon prediction errors for the vast majority of materials, highlighting its robust performance and strong capability to accurately predict phonon features across a wide variety of crystal structures. In contrast, M3GNet[43] and CHGNet[28] exhibit noticeable prediction errors for certain materials, accompanied by more pronounced variations in their performance metrics. Additionally, Fig. 7(b) illustrates the minimum and maximum values of the mean absolute error (MAE) in the phonon band structures predicted by the three models, calculated along a high-symmetry q-path.[44] Figure 5(c) presents a comparison between the phonon band structures obtained using MACE (machine learning potential model) and those computed via DFT. The close agreement between these two sets of results confirms that the dynamical features incorporated into our model are both accurate and physically meaningful, thereby validating the reliability of IGDS in capturing dynamical stability information.

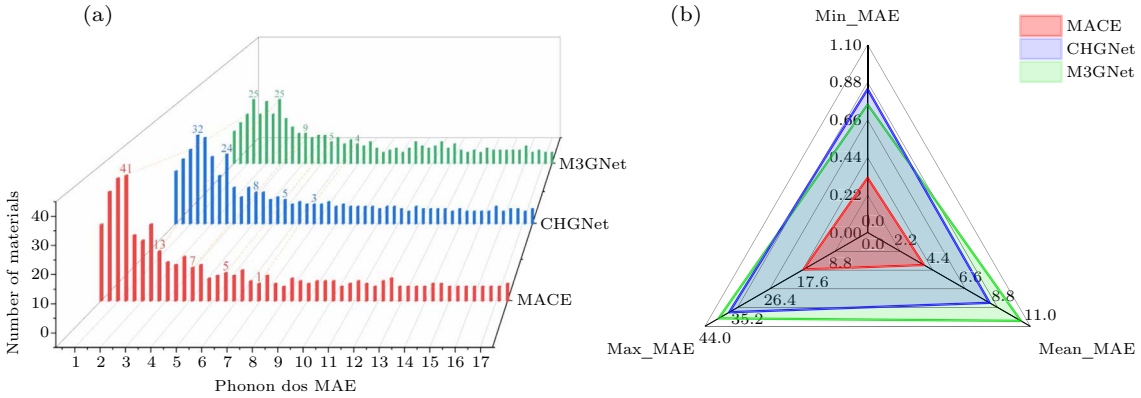


Fig. 7. Evaluation of dynamic stability feature prediction accuracy. (a) Comparison of the MAE in phonon DOS predictions for three machine-learning interatomic potential models: MACE, M3GNet, and CHGNet. (b) Comparison of the MAE in phonon band structure predictions across the same three models, highlighting the predictive performance and robustness of each method.

4. Discussion

The successful experimental synthesis of a material cannot be determined solely by its thermodynamic stability, as it also depends on factors such as kinetics, the availability of suitable precursors, and the synthesis methodologies. Nevertheless, many existing methods rely primarily on static descriptors based on composition or structure. While such representations can capture partial correlations related to thermodynamic stability (such as formation energy trends or distance to the convex hull), they inherently neglect the physical constraints that determine whether a particular phase can be obtained under experimental conditions. In addition, energy-based heuristic approaches generally lack a universal criterion for assessing synthesizability, as the appropriate threshold can vary substantially among different classes of materials owing to variations in compositional complexity and synthesis conditions.

To overcome these limitations, the proposed IGDS framework advances the predictive modeling of crystal synthesizability by integrating static structural and phonon-based dynamical information within a deep learning architecture, thereby enabling a more comprehensive understanding of the factors governing material formation. To effectively leverage the complementary nature of these two feature domains, IGDS employs a direct concatenation strategy, which preserves the full representational capacity of both static and dynamic inputs without premature information compression. This fusion enhances the model's ability to capture complex interdependencies between structure and stability. As a result, it improves predictive accuracy and overcomes the limitations of ground-state energy metrics, which often struggle to distinguish experimentally unsynthesizable low-energy polymorphs. The invariance of the crystal graph construction further ensures that model predictions remain robust against crystallographic symmetries, reinforcing the physical interpretability and generalizability of the method across diverse material classes.

Despite the promising performance of IGDS, the intri-

cate relationship between thermodynamic metastability and dynamic stability underscores the complexity of synthesizability, which likely involves additional factors beyond those captured in the current dataset and model. For instance, due to limitations in currently available public data, extrinsic synthesis conditions — such as temperature, pressure, precursor selection, and reaction kinetics — may significantly influence outcomes but remain unaccounted for in this work. Future studies will incorporate these external factors through a combination of multimodal learning frameworks and refined labeling strategies, aiming to integrate synthetic pathway data and environmental variables with existing crystal structure descriptors to enhance model robustness. Nonetheless, IGDS presents a promising approach that seeks to bridge fundamental physical principles with data-driven materials design. Its preliminary success in predicting the synthesizability of crystals highlights its potential to support future efforts in accelerated materials discovery and synthesis planning.

Data availability statement

The data used in this study are publicly available from the Materials Project database (https://materialsproject.org, version 2018.06.01) and the JARVIS database (https://jarvis.nist.gov). No new datasets were generated or deposited during the course of this study.

Acknowledgments

The authors would like to express their sincere gratitude to Mr. Xuao Li, Mr. Ao Shen, and Mr. Ning Ma for their valuable discussions and assistance with proofreading the manuscript. Their constructive feedback and support have been greatly appreciated.

References

[1] Nzereogu P U, Omah A D, Ezema F I, Iwuoha E I and Nwanya A C 2022 *Appl. Surf. Sci. Adv.* **9** 100233
[2] Li X Y, Weng S T and Lin G 2020 *Chin. Phys. B* **29** 028801
[3] Ding K, Yang T, Leung M T, Yang K, Cheng H, Zeng M, Li B and Yang M 2023 *Curr. Opin. Electrochem.* **42** 101404
[4] Jo B, Chen W and Jung H S 2025 *J. Energy Chem.* **101** 298
[5] Luo Y, Bag S, Zaremba O, Cierpka A, Andreo J, Wuttke S, Friederich P and Tsotsalas M 2022 *Angew. Chem. Int. Ed.* **61** e202200242
[6] Therrien F, Jones E B and Stevanović V 2021 *Appl. Phys. Rev.* **8** 031310
[7] Bartel C J, Millican S L, Deml A M, Rumptz J R, Tumas W, Weimer A W, Lany S, Stevanović V, Musgrave C B and Holder A M 2018 *Nat. Commun.* **9** 4168
[8] Chen J, Calvin J, Asplund M, King S W, Woodfield B F and Navrotsky A 2019 *J. Chem. Thermodyn.* **128** 320
[9] Sun W, Dacek S T, Ong S P, Hautier G, Jain A, Richards W D, Gamst A C, Persson K A and Ceder G 2016 *Sci. Adv.* **2** e1600225
[10] Aykol M, Dwaraknath S S, Sun W and Persson K A 2018 *Sci. Adv.* **4** eaaq0148
[11] Antoniuk E R, Cheon G, Wang G, Bernstein D, Cai W and Reed E J 2023 *npj Comput. Mater.* **9** 155
[12] Davariashtiyani A, Kadkhodaie Z and Kadkhodaei S 2021 *Commun. Mater.* **2** 115
[13] Zhu R, Tian S I P, Ren Z, Li J, Buonassisi T and Hippalgaonkar K 2023 *ACS Omega* **8** 8210
[14] Xie T and Grossman J C 2018 *Phys. Rev. Lett.* **120** 145301
[15] Jang J, Gu G H, Noh J, Kim J and Jung Y 2020 *J. Am. Chem. Soc.* **142** 18836
[16] Kittel C and McEuen P 2018 *Introduction to Solid State Physics* (8th edn.) (Hoboken: John Wiley & Sons)
[17] Tolborg K, Klarbring J, Ganose A M and Walsh A 2022 *Digit. Discov.* **1** 586
[18] Jain A, Ong S P, Hautier G, Chen W, Richards W D, Dacek S, Cholia S, Gunter D, Skinner D, Ceder G and Persson K A 2013 *APL Mater.* **1** 011002
[19] Schütt K T, Arbabzadah F, Chmiela S, Müller K R and Tkatchenko A 2017 *Nat. Commun.* **8** 13890
[20] Rupp M, Tkatchenko A, Müller K R and von Lilienfeld O A 2012 *Phys. Rev. Lett.* **108** 058301
[21] Gorfman S 2020 *Acta Crystallogr. A: Found. Adv.* **76** 713
[22] Choudhary K and DeCost B 2021 *npj Comput. Mater.* **7** 185
[23] Stoffel R P, Wessel C, Lumey M W and Dronskowski R 2010 *Angew. Chem. Int. Ed.* **49** 5242
[24] Wallace D C and Callen H 1972 *Am. J. Phys.* **40** 1718
[25] Giustino F 2017 *Rev. Mod. Phys.* **89** 015003
[26] Batatia I, Benner P, Chiang Y, *et al.* 2023 arXiv:2401.00096 [physics.chem-ph]
[27] Batatia I, Kovacs D P, Simm G, Ortner C and Csányi G 2022 *Advances in Neural Information Processing Systems*, November 28–December 9, 2022 New Orleans, USA, pp. 11423
[28] Deng B, Zhong P, Jun K, Riebesell J, Han K, Bartel C J and Ceder G 2023 *Nat. Mach. Intell.* **5** 1031
[29] Togo A, Chaput L, Tadano T and Tanaka I 2023 *J. Phys.: Condens. Matter* **35** 353001
[30] Togo A 2022 *J. Phys. Soc. Jpn.* **92** 012001
[31] Kingma D P and Ba J 2015 *International Conference on Learning Representations*, May 7–9, 2015 San Diego, USA, pp. 13
[32] Loshchilov I and Hutter F 2019 *International Conference on Learning Representations*, May 6–9, 2019 New Orleans, USA, pp. 11254–11263
[33] Smith L N and Topin N 2018 *International Conference on Learning Representations Workshop*, April 30–May 3, 2018 Vancouver, Canada, (Workshop paper)
[34] Chen C, Ye W, Zuo Y, Zheng C and Ong S P 2019 *Chem. Mater.* **31** 3564
[35] Hellenbrandt M 2004 *Crystallogr. Rev.* **10** 17
[36] Scheirer W J, Jain L P and Boult T E 2014 *IEEE Trans. Pattern Anal. Mach. Intell.* **36** 2317
[37] Yan K, Liu Y, Lin Y and Ji S 2022 *Advances in Neural Information Processing Systems*, November 28–December 9, 2022 New Orleans, USA, p. 15066
[38] Choudhary K, Garrity K F, Reid A C E, *et al.* 2020 *npj Comput. Mater.* **6** 173
[39] Tshitoyan V, Dagdelen J, Weston L, Dunn A, Rong Z, Kononova O, Persson K A, Ceder G and Jain A 2019 *Nature* **571** 95
[40] Wei F, Deng Z, Sun S, Hartono N T, Seng H, Buonassisi T, Bristowe P and Cheetham A 2019 *Chem. Commun.* **55** 3721
[41] Volonakis G, Haghighirad A A, Milot R L, Sio W H, Filip M R, Wenger B, Johnston M B, Herz L M, Snaith H J and Giustino F 2017 *J. Phys. Chem. Lett.* **8** 772
[42] Kegler V D and Fiscehr S C 2018 *Int. J. Adv. Eng. Res. Sci.* **5** 349
[43] Qi J, Ko T W, Wood B C, Pham T A and Ong S P 2024 *npj Comput. Mater.* **10** 43
[44] Setyawan W and Curtarolo S 2010 *Comput. Mater. Sci.* **49** 299